

# The characteristics of the 2022 Tonga volcanic tsunami in the Pacific Ocean

Gui Hu<sup>1</sup>, Linlin Li<sup>1,2</sup>, Zhiyuan Ren<sup>3</sup>, Kan Zhang<sup>1</sup>

1. Guangdong Provincial Key Laboratory of Geodynamics and Geohazards, School of Earth Sciences and Engineering, Sun Yat-sen University, Guangzhou, China

2. Southern Marine Science and Engineering Guangdong Laboratory (Zhuhai), Zhuhai, China

3. Department of Civil and Environmental Engineering, National University of Singapore, Singapore.

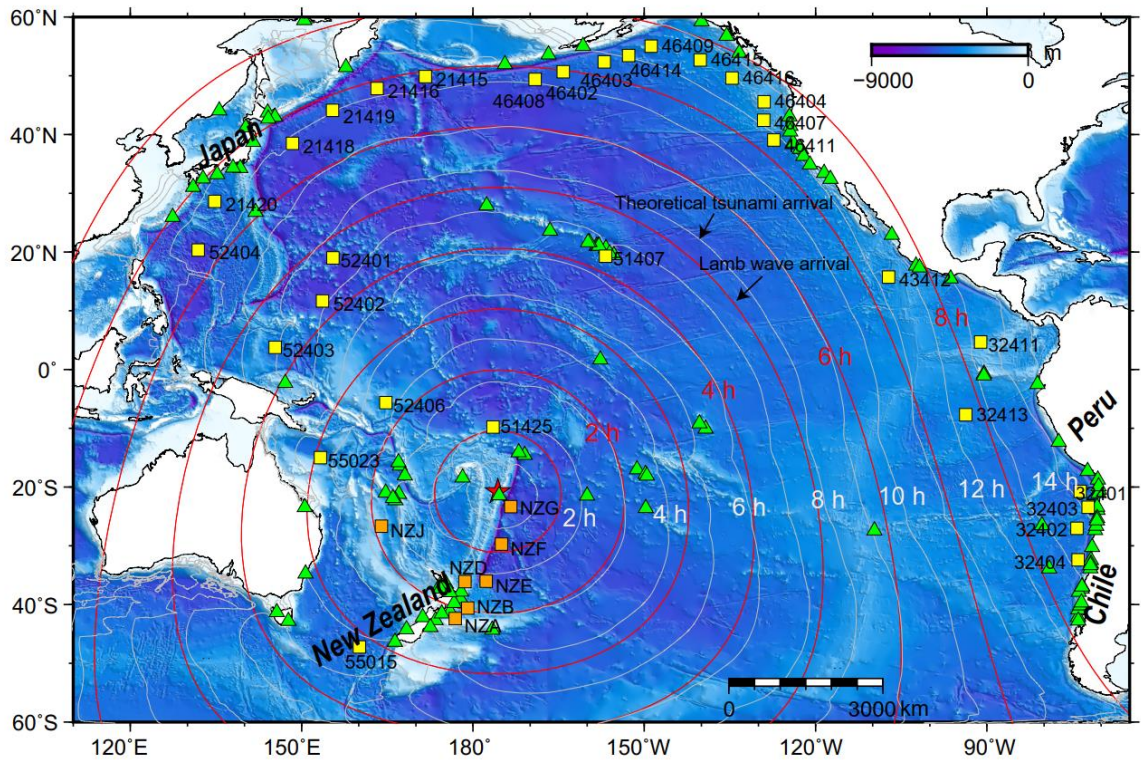
*Correspondence to:* Linlin Li (lilinlin3@mail.sysu.edu.cn)

**Abstract.** On 15th January 2022, an exceptional eruption of Hunga Tonga–Hunga Ha’apai volcano generated atmospheric and tsunami waves that were widely observed at oceans globally, gaining a remarkable attention to scientists in related fields. The tsunamigenic mechanism of this rare event remains an enigmatic due to its complexity and lacking of direct underwater observations. Here, to explore the tsunamigenic mechanisms of this volcanic tsunami event and its hydrodynamic processes in the Pacific Ocean, we conduct tsunami waveform and spectral analyses of the waveform recordings at 116 coastal gauges and 38 deep-ocean buoys across the Pacific Ocean. Combined with the constraints of some representative barometers, we obtain the plausible tsunamigenic origins during the volcano activity. We identify four distinct tsunami wave components generated by air-sea coupling and seafloor crustal deformation. Those tsunami components are differentiated by their different propagating speeds or period bands. The first-arriving tsunami component with ~80–100 min period was from shock waves spreading at a velocity of ~1000 m/s in the vicinity of the eruption. The second component with extraordinary tsunami amplitude in deep sea was from Lamb waves. The Lamb wave with ~30–40 min period radically propagated outward from the eruption site with spatially decreasing propagation velocities from ~340 m/s to ~315m/s. The third component with ~10–30 min period was probably from some atmospheric gravity wave modes propagating faster than 200 m/s but slower than Lamb waves. The last component with ~3–5 min period originated from partial caldera collapse with dimension of ~0.8–1.8 km. Surprisingly, the 2022 Tonga volcanic tsunami produced long oscillation in the Pacific Ocean which is comparable with those of the 2011 Tohoku tsunami. We point out that the long oscillation is not only associated with the resonance effect with the atmospheric acoustic-gravity waves, but more importantly the interactions with local bathymetry. This rare event also calls for more attention to the tsunami hazards produced by atypical tsunamigenic source, e.g., volcanic eruption.

## 30 1. Introduction

31 On 15 January 2022 at 04:14:45 (UTC), a submarine volcano erupted violently at the uninhabited Hunga  
32 Tonga-Hunga Ha'apai (HTHH) island at 20.546°S 175.390°W (USGS, 2022). The volcano is located ~67  
33 km north of Nuku'alofa, the capital of Tonga (NASA, 2022) (Figure 1). The blasts launched plumes of  
34 ash, steam, and gas ~58 km high into stratosphere (Yuen et al., 2022) which not only blanketed nearby  
35 islands in ash (Duncombe, 2022; NASA, 2022), but caused various atmospheric acoustic-gravity wave  
36 modes (AGWs) of various scales, e.g., Lamb waves from atmospheric surface pressure disturbance  
37 associated with the eruption (Liu and Higuera, 2022; Adam, 2022; Kubota et al., 2022; Matoza et al.,  
38 2022). Tsunami with conspicuous sea level changes were detected by coastal tide gauges and Deep-ocean  
39 Assessment and Reporting of Tsunamis (DART) buoy stations in the Pacific (Figure 1), the Atlantic, and  
40 Indian Oceans as well as the Caribbean and Mediterranean seas (Carvajal et al., 2022; Kubota et al., 2022;  
41 Ramírez-Herrera et al., 2022), while the large waves were mainly concentrated in the Pacific Ocean, like  
42 coastlines of New Zealand, Japan, California, and Chile (Carvajal et al., 2022). The event caused at least  
43 3 fatalities in Tonga. Two people drowned in northern Peru when ~2 m destructive tsunami waves  
44 inundated an island in the Lambayeque region, Chile (Edmonds, 2022).

45 Satellite images revealed that the elevation of HTHH island has gone through dramatic change before  
46 and after the mid-January 2022 eruption. Previously, after the 2015 eruption, the two existing Hunga  
47 Tonga and Hunga Ha'apai Islands were linked together. The volcanic island rose 1.8 km from the seafloor  
48 where it stretched ~20 km across and topped a underwater caldera ~5 km in diameter (Garvin et al., 2018;  
49 NASA, 2022). After the violent explosion on 15 January 2022, the newly formed island during 2015 was  
50 completely gone, with only small tips left in far southwestern and northeastern HTHH island (NASA,  
51 2022). HTHH volcano lies along the northern part of Tonga–Kermadec arc, where the Pacific Plate  
52 subducts under the Indo-Australian Plate (Billen et al., 2003). The convergence rate (15~24 cm/year)  
53 between the Tonga–Kermadec subduction system and the Pacific plate is among the fastest recorded plate  
54 velocity on Earth, forming the second deepest trench around the globe (Satake, 2010; Bevis et al., 1995).  
55 The fast convergence rate contributes to the frequent earthquakes, tsunamis and volcanic eruptions in  
56 this region historically (Bevis et al., 1995). The 2022 HTHH volcano is part of a submarine-volcano  
57 chain that extends all the way from New Zealand to Fiji (Plank et al., 2020). HTHH volcano had many  
58 notable eruptions before 2022 since its first historically recorded eruption in 1912, i.e., in 1937, 1988,



60  
 61 **Figure 1. The spatial distribution of the eruption site (red star), DART stations (squares), tide**  
 62 **gauges (triangles) and the calculated tsunami arrival times. White contours indicate the modelled**  
 63 **arrival times of conventional tsunami. Red contours indicate the estimated arrival times of Lamb**  
 64 **waves (see how we derive these contours in section 3.1).**

65 The 2022 HTHH eruption is the first volcanic event which generates worldwide tsunami signatures since  
 66 the 1883 Krakatau event (Matoza et al., 2022; Self and Rampino, 1981; Nomanbhoy and Satake, 1995).  
 67 The tsunamigenic mechanism of this rare volcanic eruption-induced tsunami is still poorly understood  
 68 due to its complex nature and the deficiencies of near-field seafloor surveys. Various tsunami generation  
 69 mechanisms have been proposed so far based on the observations of ground-based and spaceborne  
 70 geophysical instrumentations (Kubota et al., 2022; Matoza et al., 2022; Carvajal et al., 2022). The  
 71 mechanisms are closely associated with the air-sea coupling with atmospheric waves. Atmospheric  
 72 waves propagating in the atmospheric fluid with different speeds are generated by different physical  
 73 mechanisms (E. E. Gossard and W. H. Hooke, 1975). Nonlinearities in the process may lead to the  
 74 formation of shock-wave and period lengthening. The balance between gravity and buoyancy causes  
 75 gravity waves. The acoustic wave propagate by atmospheric fluid compression and rarefaction (Matoza  
 76 et al., 2022). The most-mentioned mechanism of the tsunami is the fast-traveling atmospheric Lamb wave  
 77 generated by the atmospheric pressure rise of  $\sim 2$  hPa during the eruption. The Lamb wave circled the

78 Earth for several times with travelling speed close to that of the sound wave in the lower atmosphere,  
79 leading to globally observed sea level fluctuations (Adam, 2022; Duncombe, 2022; Kubota et al., 2022;  
80 Matoza et al., 2022) (Figure 1). The second mechanism is suggested to be a variety of other acoustic-  
81 gravity wave modes (Adam, 2022; Matoza et al., 2022; Themens et al., 2022; Zhang et al., 2022). The  
82 third mechanism may be related to the seafloor crustal deformation induced by one or more volcanic  
83 activities in the vicinity of the eruption site (e.g., pyroclastic flows, partial collapse of the caldera)  
84 (Carvajal et al., 2022) , which are more responsible for the near-field tsunamis with theoretical tsunami  
85 speeds.

86 To investigate the possible tsunamigenic mechanisms and detailed hydrodynamic behaviors of this rare  
87 volcanic tsunami event, in this study, we collect, process and analyze the sea level measurements from  
88 116 tide gauge and 38 DART buoys in the Pacific Ocean (shown in Figures 1 and 2). We first do statistical  
89 analysis of the tsunami waveforms to estimate the propagating speed of the Lamb wave and to understand  
90 the tsunami wave characteristics in the Pacific Ocean through demonstrating the tsunami wave properties,  
91 i.e., arrival times, wave heights and durations. We then conduct wavelet analysis for representative DART  
92 buoys and tide gauges respectively to explore tsunamigenic mechanisms of the event and to better  
93 understand its hydrodynamic processes in the Pacific Ocean. Aided by wavelet analysis of corresponding  
94 barometers near the selected DART buoys and comparison with tsunami records of the 2011 Tohoku  
95 tsunami, we are able to piece together all the analysis and demonstrate that the 2022 HTHH tsunami was  
96 generated by air-sea coupling with a wide range of atmospheric waves with different propagating  
97 velocities and period bands, and seafloor crustal deformation associated with the volcanic eruption. We  
98 demonstrate as well that the tsunami was amplified at the far-field Pacific coastlines where the local  
99 bathymetric effects play a dominant role in tsunami scale.

## 100 **2. Data and Methods**

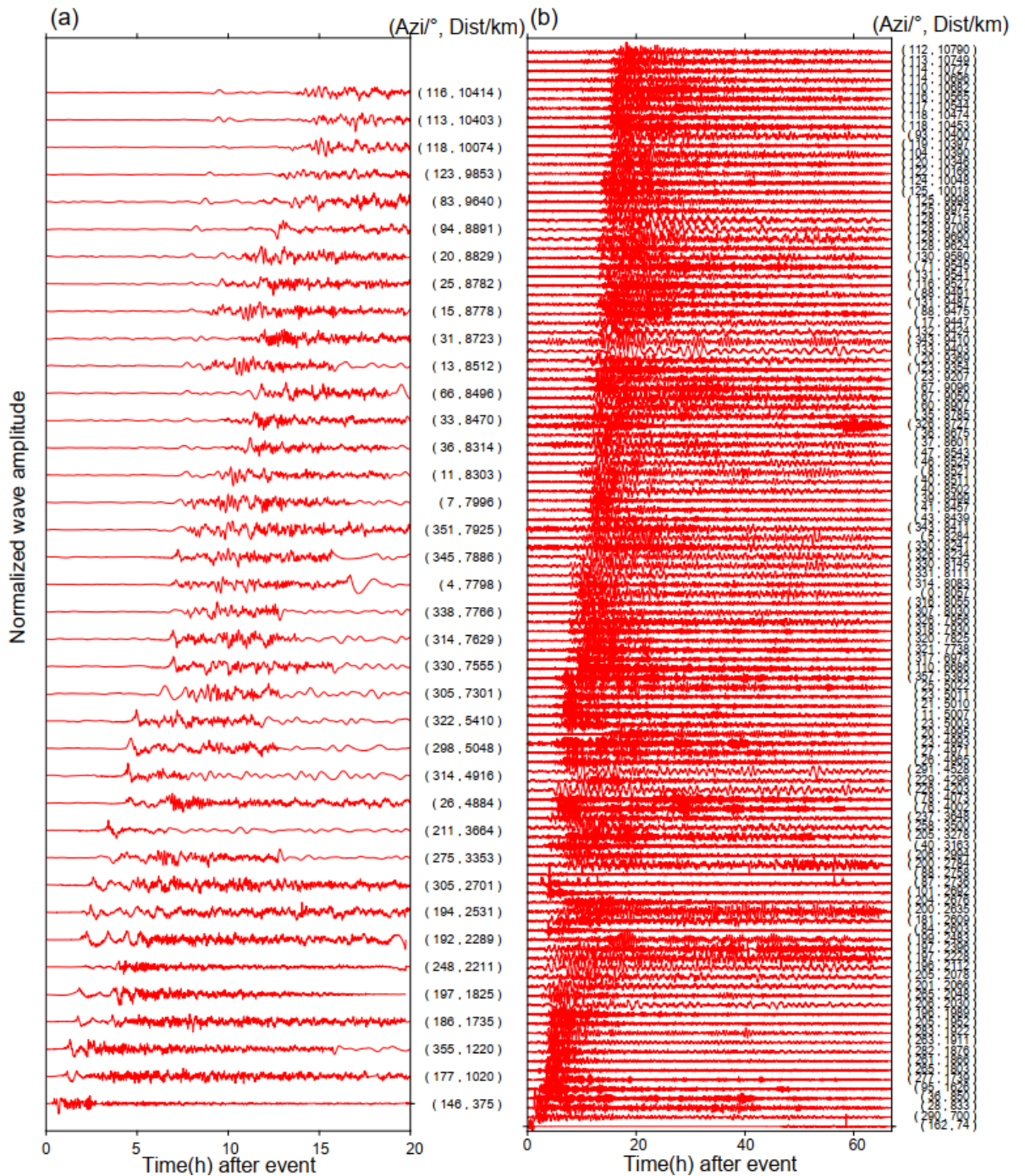
### 101 **2.1 Data**

102 We collected high-quality sea level records across the Pacific Ocean at 38 DART buoys (in which 31  
103 stations from <https://nctr.pmel.noaa.gov/Dart/>, 7 stations from <https://tilde.geonet.org.nz/dashboard/>) and  
104 116 tide gages from IOC (The Intergovernmental Oceanographic Commission, [http://www.ioc-](http://www.ioc-sealevelmonitoring.org)  
105 [sealevelmonitoring.org](http://www.ioc-sealevelmonitoring.org)) (Figure 1). The epicentral distances of tide gauges and DART buoys range

106 between 74–10790 km and 375–10414 km, respectively. The sampling rates of DART buoys are  
107 changing over time. Passing of tsunami event generally can trigger the DART system to enter its high  
108 frequency sampling mode (15 seconds or 1 min) from normal frequency mode (15 min)  
109 ([www.ndbc.noaa.gov/dart](http://www.ndbc.noaa.gov/dart)). In contrast, sampling rates of normal tide gauges at coasts are uniform with  
110 sampling interval of 1 min. The sampling interval of both DART and tide gauges is preprocessed to 15  
111 seconds. Firstly, we eliminate abnormal spikes and fill gaps by linear interpolation. Secondly, we applied  
112 a fourth-order Butterworth-Highpass filter with a cut-off frequency of  $3.5 \times 10^{-5}$  Hz ( $\sim 8$  hours) to remove  
113 the tidal components (Figure 2) (Heidarzadeh and Satake, 2013). After the two steps, quality control step  
114 is conducted to select high-quality data, in which we delete waveforms with spoiled data or massive data  
115 loss due to equipment failure, or with the maximum tsunami heights of tide gauges less than 0.2 m, then  
116 the selected data will be ready for further statistics and spectral analysis. We also collect and analyze the  
117 atmospheric pressure disturbance data recorded by some representative barometers. The sampling rates  
118 of the barometers is generally uniform with a sampling rate of 1 min except for some stations in New  
119 Zealand with interval of 10 min. Considering the sample rate, we employ a fourth-order Butterworth-  
120 Bandpass filter with period ranging between 2–150 min for wavelet analysis of the barometers with 1  
121 min sample rate, while we apply the fourth-order Butterworth-Bandpass filter with range of 30–150 min  
122 to long-period waveform display based on two reasons. (1) The barometer data we use for the analysis  
123 include some in New Zealand with 10 min sample rate; (2) Filtering out the short-period waves helps  
124 highlight long-period tsunami wave components.

125 The tsunami waveforms recorded by DART buoys which are installed offshore in the deep water are  
126 expected to contain certain characteristics of the tsunami source (Wang et al., 2020, 2021). The  
127 waveforms recorded by tide gauge distributed along coastlines are significantly influenced by local  
128 bathymetry/topography which are used for investigating bathymetric effect on tsunami behaviors  
129 (Rabinovich et al., 2017, 2006; Rabinovich, 2009). Therefore, we use the DART data for source-related  
130 analysis and choose some tide gauge data to investigate the tsunami behaviors at the Pacific coastlines.

131



132

133 **Figure 2. Detided tsunami waveforms at (a) DART buoys and (b) tide gauges. Waveforms in both**  
 134 **subplots are shown in ascending distance. Azi stands for azimuth.**

135 **2.2 Tsunami Modelling**

136 We use a numerical tsunami modelling package JAGURS (Baba et al. 2015) to simulate the tsunami  
 137 propagation of the 2022 HTHH event and obtain the theoretical tsunami arrival time based on the shallow  
 138 water wave speed (white contours in Figure 1). The code solves linear Boussinesq-type equations in a  
 139 spherical coordinate system using a finite difference approximation with the leapfrog method. We specify

140 a unit Gaussian-shaped vertical sea surface displacement at the volcanic base as the source of  
141 conventional tsunami. For a unite source  $i$  with center at longitude  $\varphi_i$  and latitude  $\theta_i$ , the  
142 displacement distribution  $Zi(\varphi, \theta)$  can be expressed as:

$$143 \quad Zi(\varphi, \theta) = \exp\left[-\frac{(\varphi-\varphi_i)^2+(\theta-\theta_i)^2}{2\sigma}\right] \quad (1)$$

144 Where we set characteristic length  $\sigma$  as 5 km (NASA, 2022). The bathymetric data is resampled from the  
145 GEBCO 2019 with 15 arc-sec resolution (The General Bathymetric Chart of the Oceans, downloaded  
146 from <https://www.gebco.net>).

### 147 **2.3 Spectral Analysis of Tsunami Waves**

148 To investigate the temporal changes of the dominant wave periods, we conduct continuous wavelet  
149 transformation (frequency-time) analyses for some representative DART buoys, tide gauges and  
150 barometers, in which wavelet Morlet mother function is implemented (Kristeková et al., 2006). The first  
151 32-hour time series of DART buoys and barometers after the eruption (at 04:14:45 on 15 January 2022)  
152 are used for source-related wavelet analysis. The first 48-hour time series of tide gauges after the eruption  
153 are employed for hydrodynamics-related wavelet analysis at coastlines. We adopt the Averaged-Root-  
154 Mean-Square (ARMS) method as a measure of absolute average tsunami amplitude with a moving time  
155 window of 20 min to calculate the tsunami duration (Heidarzadeh and Satake, 2014). We define the time  
156 durations as the time period where ARMS levels of tsunami waves are above those prior to the tsunami  
157 arrivals.

## 158 **3. Results**

### 159 **3.1 The decreasing propagation velocities of the Lamb Wave**

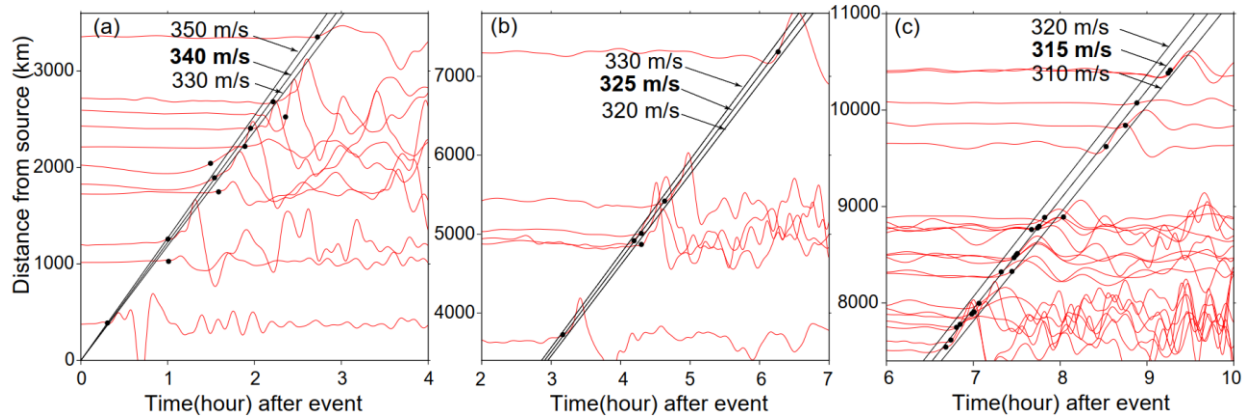
160 Although many types of atmospheric waves were generated by the 2022 HTHH eruption, the most  
161 prominent signature was the Lamb waves which were globally observed by ground-based and spaceborne  
162 geophysical instrumentations (Kulichkov et al., 2022; Liu et al., 2022; Lin et al., 2022; Matoza et al.,  
163 2022; Themens et al., 2022; Adam, 2022; Kubota et al., 2022). Interestingly, we notice that a wide range  
164 of the velocities from 280 m/s to 340 m/s were proposed through observations and Lamb wave modelling  
165 (e.g., Kubota et al., 2022; Lin et al., 2022; Matoza et al., 2022; Themens et al., 2022). The travelling  
166 velocity of Lamb waves in real atmosphere is affected by temperature distributions, winds and dissipation

167 (Otsuka, 2022). To investigate whether the propagation speeds of the lamb wave change in space and  
 168 time, we analyze the waveforms recorded by the DART buoys in the Pacific Ocean. DART buoy with  
 169 pressure sensor deployed at the ocean's bottom records the sea level change that is transferred from  
 170 pressure records in Pascals, instead of direct water height. For the 2022 HTHH tsunami event, the  
 171 pressure fluctuation at DART buoy is a superposition of the pressure changes caused by tsunami and the  
 172 Lamb wave (Kubota et al., 2022). The Pacific DART buoys recorded the most discernible air-sea  
 173 coupling pulse in deep ocean with Lamb waves that arrived earlier than the theoretical tsunamis (Figure  
 174 1). The tsunami waveforms recorded by tide gauges did not clearly detect the tsunami signals associated  
 175 with the Lamb waves, therefore are not sufficient for further analysis (Figure 2). Thus, we estimate the  
 176 speed of Lamb waves using the waveforms recorded by the Pacific DART buoys. The Lamb wave  
 177 arrivals are limited within arrival time range from possible velocities of 280–340 m/s. The time points at  
 178 which the tsunami amplitudes first exceed 1 e-4 m above sea level are defined as Lamb wave arrivals.  
 179 By carefully fitting the arrivals with different constant velocities, we illustrate the velocities of Lamb  
 180 wave were generally uniform, but slightly decrease with the increase of propagation distance (Figure 3).  
 181 The Lamb waves initially propagated radially at speed of ~340 m/s before slowing to ~325 m/s after  
 182 reaching ~3400 km, and further decreasing to ~315 m/s at 7400 km. In an isothermal troposphere  
 183 assumption, the phase velocity of the Lamb wave ( $C_L$ ) can be estimated with the following equation  
 184 (Gossard and Hooke, 1975):

$$185 \quad C_L = \sqrt{\frac{\gamma \cdot R \cdot T}{M}} \quad (2)$$

186 Where  $\gamma = 1.4$  (air specific heat ratio corresponding to atmospheric temperature),  $R = 8314.36 \text{ J kmol}^{-1}$   
 187  $\text{K}^{-1}$  (the universal gas constant),  $M = 28.966 \text{ kg kmol}^{-1}$  (molecular mass for dry air) are constant for the  
 188 air,  $T$  is the absolute temperature in kelvin. Thus, Lamb wave velocity is mainly affected by the air  
 189 temperature, meaning the travelling velocity of lamb waves might decrease when propagating from  
 190 regions with high temperature towards those with low temperatures, e.g., the north pole. By assuming a  
 191 set of possible temperatures in January (Table 1), we calculated the velocities  $C_L$  could range between  
 192 312–343 m/s when temperatures vary between -30–20 °C. Therefore, the decreased velocity of the Lamb  
 193 waves could be a consequence of cooling of the air temperature.





194  
 195 **Figure 3. Fitting the arrival times of normalized Lamb waveforms with different velocities. Black**  
 196 **dots mark the arrival times of the Lamb waves. Black lines represent velocities.**

197 **Table 1. Estimated Lamb wave velocities in an isothermal troposphere assumption**

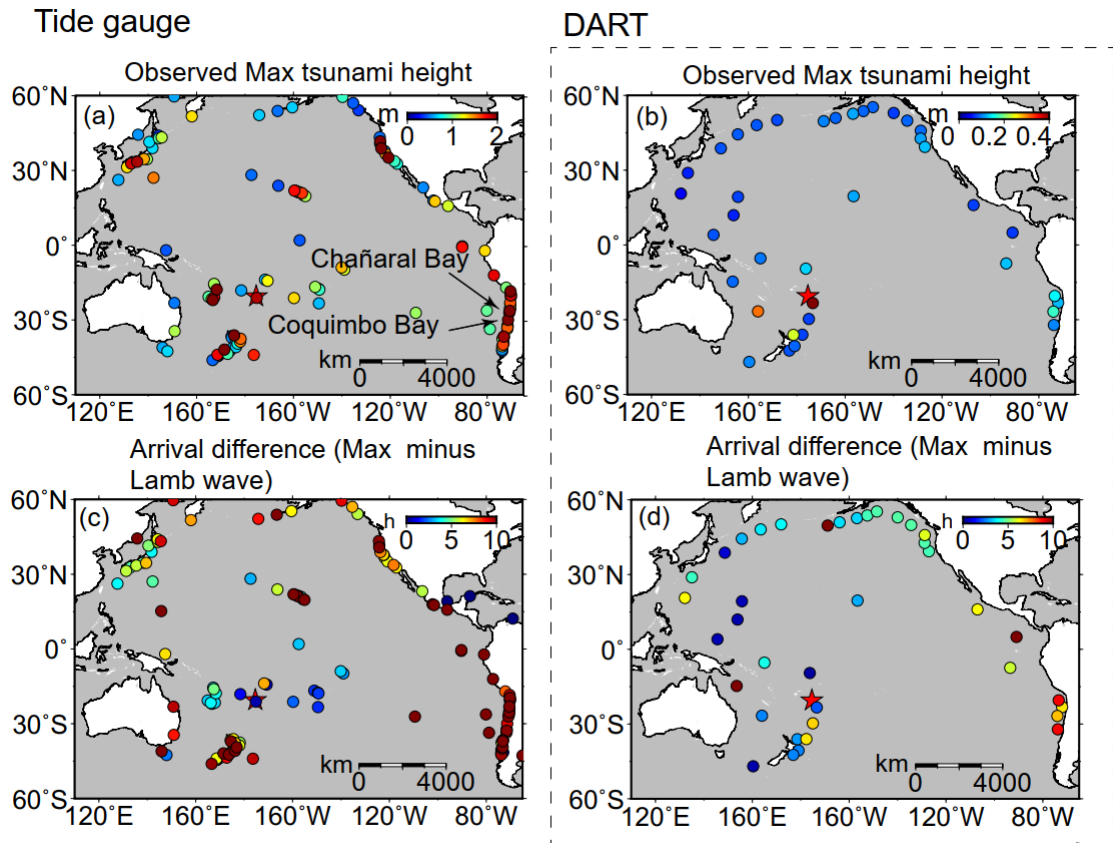
Celsius temperature (°C)	thermodynamic temperature (K)	$C_L$ (m/s)
20	293.15	343.14
10	283.15	337.23
0	273.15	331.21
-10	263.15	325.19
-20	253.15	318.86
-30	243.15	312.49

198 **3.2 Tsunami features observed by DART buoys and Tide gauges**

199 The statistics of tsunami heights and arrival times recorded at 38 DART buoys and 116 tide gauges across  
 200 the Pacific Ocean are used to interpret the tsunami characteristics. The comparison of the statistical  
 201 characters between DART and tide gauge observations yields some useful information of the  
 202 hydrodynamic process of tsunami propagation and help identify tsunami wave components with different  
 203 traveling velocities.

204 The average value of the maximum tsunami wave height (trough-to-crest) for the 116 tide gauge stations  
 205 is ~1.2 m. Figure 4a shows tide gauges with large tsunami heights exceeding 2 m are mainly distributed  
 206 in coastlines with complex geometries (Figure S1a), such as gauges at New Zealand, Japan, and north  
 207 and south America. For example, the largest tsunami height among tide gauges is 3.6 m at a bay-shaped  
 208 coastal area Chañaral in Chile (Figure S1b). In sharp contrast to tide gauges, the maximum tsunami  
 209 heights of most Pacific DART buoys are less than 0.2 m. The largest tsunami height in the DART buoys  
 210 is only ~0.4 m recorded at the nearest one, 375 km from the volcano (Figure 4b). The comparison between  
 211 DART buoys and tide gauges indicate that the direct contribution of air-sea coupling to the tsunami

212 heights is probably in the level of tens of centimeters (Kubota et al., 2022). The meter-scale tsunami  
213 heights at the coastlines suggest the bathymetric effect could play a major role during tsunami  
214 propagation. In respect to the arrival of maximum tsunami waves, the time lags between Lamb waves  
215 and the maximum heights of tide gauges mainly range between ~0–10 h (Figure 4c). The delayed times  
216 of ~10 h are observed in New Zealand, Hawaii, and west coast of America (Figure 4c), suggesting the  
217 interaction between tsunami waves and local topography/bathymetry delays the arrival of the maximum  
218 waves (e.g., Hu et al., 2022). For example, the delayed maximum tsunami height can be attributed to the  
219 edge waves (Satake et al., 2020) and resonance effect (Wang et al., 2021) from tsunami interplays with  
220 bays/harbors, islands, and continental shelves of various sizes. The significant regional dependence of  
221 the coastal tsunami heights and the time lags of the maximum tsunami waves can be attributed to the  
222 complexity of local bathymetry, such as continental shelves with different slopes, and harbor/bay with  
223 different shapes and sizes (Satake et al., 2020). On the other hand, since the DART records are less  
224 influenced by bathymetric variation in space, the first waves in DART buoys are supposed to be the  
225 maximum tsunami waves as observed in the 2011 Tohoku tsunami event (Heidarzadeh and Satake, 2013).  
226 However, we observe the inconsistency between the arrivals of the Lamb waves and the maximum  
227 tsunami heights (Figure 4d). The time lags of the maximum waves of DART buoys present a coarsely  
228 increasing tendency with the increasing distance from the volcano, which indicates the contribution of  
229 other tsunami generation mechanism propagating with a uniform but lower speed than Lamb wave.



230

231

**Figure 4. The spatiotemporal signatures of the 2022 HTHH tsunami across the Pacific Ocean. (a) Observed the maximum tsunami height (trough-to-crest height) of tide gauges. (c) Arrival differences between the maximum tsunami height of tide gauges and Lamb waves. (b) and (d) are the same as (a) and (c) but for DART buoys.**

234

235

### 3.3 Tsunami components identified from wavelet analysis

236

The statistical analysis of tsunami waveforms at tide gauges and DART buoys suggest the tsunami waves

237

likely contain several components with different source origins. To further identify these tsunami

238

components, we conduct wavelet analysis for tsunami waveforms recorded by representative DART

239

buoys and air pressure waveforms recorded by selected barometers. We demonstrate the analysis result

240

through the frequency-time (f-t) plot of wavelet which shows how energy and period vary at frequency

241

and time bands (Figure 5 and Figure 6). Tsunami components have clear signatures in all f-t plots as the

242

energy levels are quite large when they arrive. Figure 5 shows the wavelet analysis of six DART buoys

243

located in the vicinity of the eruption site (<3664 km). Figure 6 show the wavelet analysis of ten DART

244

buoys located in the Pacific rim which are far away from the source location. We observe three interesting

245

phenomena: 1) most of the tsunami wave energy is concentrated in four major period bands, i.e., 3–5

246

min, ~10–30 min, ~30–40 min, and ~80–100 min; 2) The significant tsunami component with period

247 band of 3-5 mins are recorded by stations between the eruption site and the north tip of the New Zealand;  
 248 3) There exists one exceptional tsunami component with longer wave period of ~80–100 min mainly  
 249 recorded in the Tonga, the New Zealand and Hawaii, which travels even faster than the Lamb waves.  
 250 To further explore the source mechanism of these tsunami components, we take advantage of the  
 251 published information related to different propagating velocities of atmospheric gravity waves (Kubota  
 252 et al., 2022) and add four kinds of propagating velocities as criteria to differentiate the tsunami arrivals  
 253 from different sources (Figure 5 and Figure 6). The first reference speed is 1000 m/s related to the  
 254 radically propagating atmospheric shock waves near the source region (Matoza et al., 2022; Themens et  
 255 al., 2022). The second one is the velocities of Lamb wave ranging between 315–340 m/s derived from  
 256 the aforementioned analysis in section 3.1 (Figure 3). The third one is 200 m/s corresponding to the lower  
 257 limit of atmospheric gravity wave modes other than Lamb waves which were also excited by the volcanic  
 258 eruptions (Kubota et al., 2022). The last is the arrival time of conventional tsunami given by tsunami  
 259 modelling (Figure 1). The theoretical velocity of conventional tsunami is significantly nonuniform  
 260 spatially as compared with those of the atmospheric waves. The conventional tsunami propagation speed  
 261 is determined by the water depth along the propagation route. The velocity of non-dispersion shallow-  
 262 water waves ( $C_H$ ) in the ocean is given by:

$$263 \quad C_H = \sqrt{g \cdot H} \quad (3)$$

264 Where  $g$  is gravity acceleration ( $9.81\text{m/s}^2$ ),  $H$  is the water depth. The propagation velocities of tsunami  
 265 are ~296–328 m/s in the deepest trenches on earth (i.e., ~11 km in Mariana Trench and ~9 km in Tonga  
 266 Trench). The velocities decrease quickly to only ~44 m/s at ~200 m depth along the edge of continental  
 267 shelf. With the average depth of ~4–5 km, the average velocities in the Pacific Ocean range between  
 268 ~198–221 m/s. Thus, theoretical tsunami velocities present significant slowness and variability. We  
 269 delineate the arrival times of the four reference speeds in Figures 5 and 6.

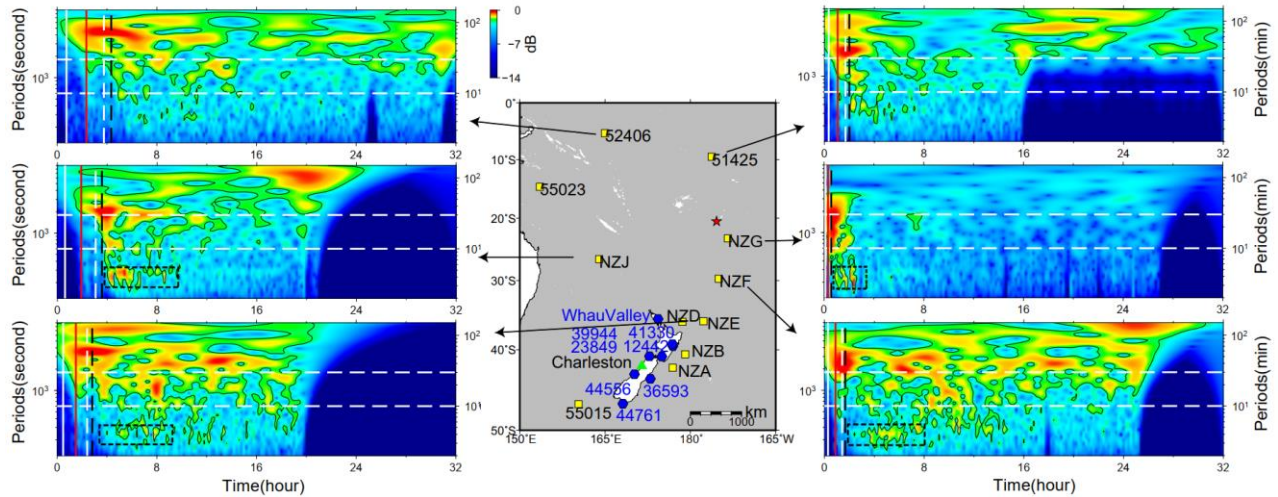
270 One particularly remarkable phenomenon is that the wave component with period of ~80–100 min  
 271 propagated at a very fast speed of ~1000 m/s in the vicinity of the HTHH site, i.e., New Zealand and  
 272 Hawaii (e.g., stations 52406, NZJ, NZE, 51425 in Figure 5, and 51407 in Fig. 6). We infer that the  
 273 tsunami component within ~80–100 min period band was likely produced by the atmospheric shock  
 274 waves during the initial stage of the volcanic eruption and spatially only cover the near-source region.  
 275 To verify this observation, we select 16 representative barometers located in the near-source region and

276 far-field area for wavelet analysis (see the locations in Figure 5 and Figure 6). Figure 7 shows the  
277 waveforms of atmospheric pressure at selected locations and Figure 8 provides the frequency-time (f-t)  
278 plot of wavelet analysis of some representative barometers. Interestingly, we are able to discern the air  
279 pressure pulses prior to Lamb waves at barometers in New Zealand (the two columns on the left in Figure  
280 7), although such signals are not detectable in waveforms recorded by barometers far from the source  
281 (the two columns on the right in Figure 7). The spatial distribution of such unusual pressure changes  
282 suggest that the fast travelling shock waves were only limited in the near-source region, as reflected in  
283 the travelling ionospheric disturbances (Matoza et al., 2022; Themens et al., 2022). Additionally, we also  
284 see that the long period signals of ~80–100 min appear in DART buoys far away from the eruption site.  
285 Such signals may be related with the long-period gravity waves (Matoza et al., 2022).

286 The tsunami components at period band of ~30–40 min can be readily associated with Lamb waves  
287 because the arrival times of tsunami waves and Lamb waves have excellent match, as shown in the  
288 tsunami data recorded by DART buoys (e.g., NZJ and 51425 in Figure 5; 51407, 32401 and 32413 in  
289 Figure 6) and pressure data by barometers (Figure 8).

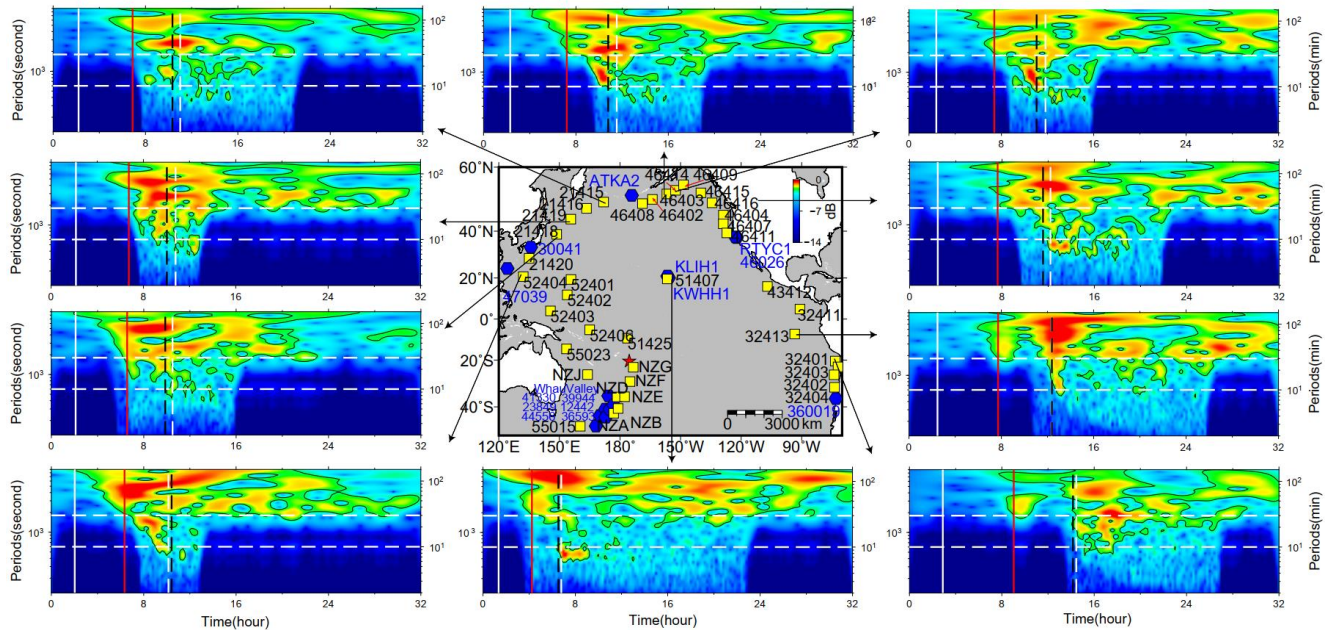
290 For the tsunami components with the period band of ~10–30 min, although the arrivals of ~10–30 min  
291 tsunami components cover some theoretical tsunami arrival times, they do not consistently match. The  
292 tsunami components occurring within the time period between Lamb waves and the lower gravity waves’  
293 velocities has a good agreement with the velocity range of several atmospheric gravity wave modes  
294 (Matoza et al., 2022; Themens et al., 2022; Kubota et al., 2022). Similarly, the air pressure data also show  
295 energy peaks at ~10–30 min period band, which is consistent with the tsunami data (Figure 8). Such  
296 consistency further verifies the contribution of atmospheric gravity waves to the volcanic tsunami.

297 The tsunami components with the shortest period of ~3–5 min (stations NZE, NZF, NZG and NZJ;  
298 marked with black dashed squares in Figure 5) are only observed at DART records near the eruption  
299 location. Meanwhile, the arrival times of these components agree well with the modelled arrivals of  
300 conventional tsunami. Thus, we believe the observed shortest period band should originate from the  
301 seafloor crustal deformation. We further infer that this component could be generated by the partial  
302 underwater caldera collapse and/or subaerial/submarine landslide failures associated with 2022 HTHH  
303 volcanic eruption.



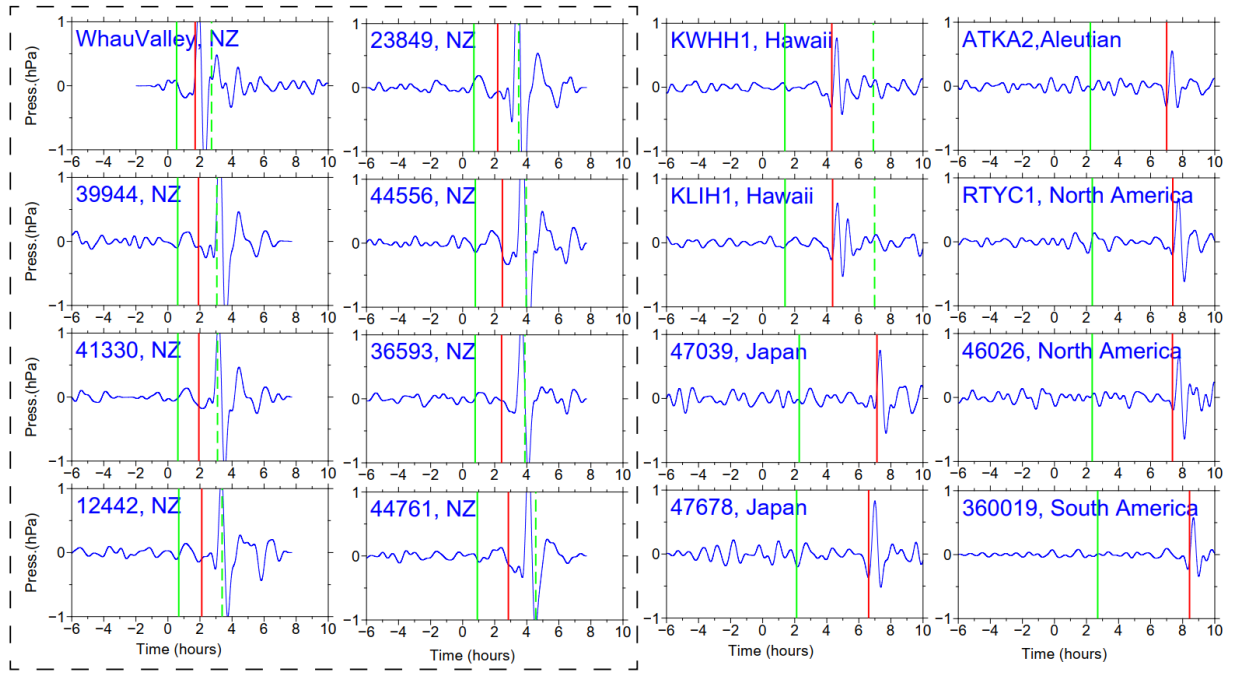
304

305 **Figure 5. Wavelet analysis of representative DART buoys in the vicinity of the HTHH volcano. In**  
 306 **each sub-plot, the solid vertical white lines mark the arrival time with travelling velocity of 1000**  
 307 **m/s. The solid vertical red lines mark the arrivals of Lamb waves. The dashed vertical white lines**  
 308 **mark lower limit of AGWs' velocity of 200 m/s (Kubota et al., 2022). The dashed vertical black**  
 309 **lines represent the theoretical tsunami arrivals. The dashed horizontal white lines mark two**  
 310 **reference wave periods of 10 min and 30 min. The blue hexagons represent the locations of**  
 311 **barometers. Green triangle makes the location of the tide gauges at Charleston.**



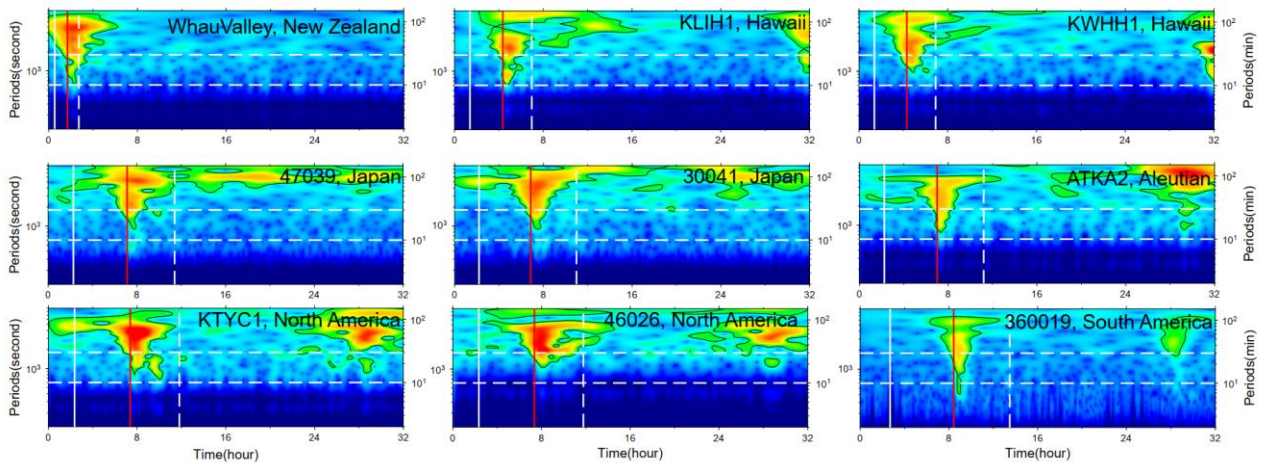
312

313 **Figure 6. Wavelet analysis of representative DART buoys far away from the HTHH volcano. In**  
 314 **each sub-plot, the solid vertical white lines mark the arrival time with travelling velocity of 1000**  
 315 **m/s. The solid vertical red lines mark the arrivals of Lamb waves. The dashed vertical white lines**  
 316 **mark lower limit of AGWs' velocity of 200 m/s. The dashed vertical black lines represent the**  
 317 **theoretical tsunami arrivals. The dashed horizontal white lines mark two reference wave periods**  
 318 **of 10 min and 30 min. The blue hexagons represent the locations of barometers.**



319

320 **Figure 7. Shockwave-related atmospheric pressure waveforms of selected barometers in the Pacific**  
 321 **Ocean. All traces have been filtered between 30 min and 150 min. In each sub-plot, the solid vertical**  
 322 **green lines mark the arrival time with travelling velocity of 1000 m/s. The solid vertical red lines**  
 323 **mark the arrivals of Lamb waves. The dashed vertical green lines mark lower limit of AGWs'**  
 324 **velocity of 200 m/s.**



325

326 **Figure 8. Wavelet analysis of some representative barometers. In each sub-plot, the solid vertical**  
 327 **white lines mark the arrival time with travelling velocity of 1000 m/s. The solid vertical red lines**  
 328 **mark the arrivals of Lamb waves. The dashed vertical white lines mark lower limit of AGWs'**  
 329 **velocity 200 m/s. The dashed horizontal white lines mark three reference periods of 10 min and 30**  
 330 **min.**

331 **4. Discussion**

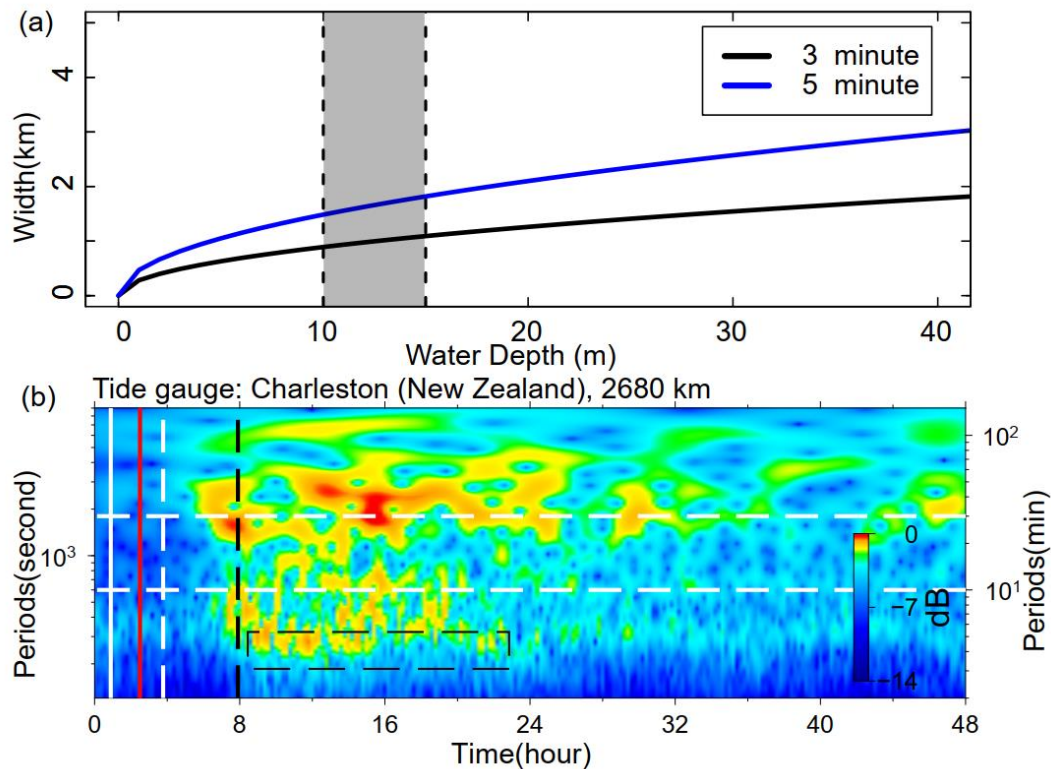
332 **4.1 Tsunami from Caldera Collapse and Its Long-distance Traveling Capability**

333 The tsunami wave energy distributed in different period bands is identified with reference arrival times.  
334 The tsunami component with 3–5 min period is most likely generated by seafloor crustal deformation in  
335 the volcanic site, but specific mechanism is not determined. A variety of possible scenarios associated  
336 with the eruption could be responsible for the near-field tsunami waves, such as volcanic earthquakes,  
337 pyroclastic flows entering the sea, underwater caldera flank collapse, and subaerial/submarine failures  
338 (Self and Rampino, 1981; Pelinovsky et al., 2005). To further investigate the source mechanism, we  
339 apply a simplified model (Rabinovich, 1997) to estimate the probable dimension of tsunami source:

340 
$$L = \frac{T\sqrt{gH}}{2} \quad (4)$$

341 Where  $L$  is the typical dimension (length or width) of the tsunami source,  $H$  is average water depth in the  
342 source area,  $g$  is the gravity acceleration, and  $T$  is primary tsunami period. By comparing with the post-  
343 2015 morphology of the HTHH caldera which was obtained through drone photogrammetry and  
344 multibeam sounder surveys, Stern et al. (2022) estimate that much of the newly-formed Hunga Tonga  
345 Island and the 2014/2015 cone were destroyed by the 2022 eruption, and the vertical deformation of  
346 Hunga Ha'apai Island is ~10–15 m (Stern et al., 2022). With no more quantitative constraint of the  
347 seafloor deformation, we tentatively assume  $H$  as 10–15 m, then the possible dimension of seafloor  
348 crustal deformation responsible for the small-scale tsunami could be in the scale of 0.8–1.8 km (Figure  
349 9a). The estimated size is very likely from partial caldera collapse that usually has limited scale in  
350 volcanic site (Ramalho et al., 2015; Omira et al., 2022). If it is the case, the partial flank collapse could  
351 be located between Hunga Tonga and Hunga Ha'apai Islands.





352

353 **Figure 9. Mechanism of tsunami component with 3–5min period. (a) The source dimension**  
 354 **estimated by equation 4. (b) Wavelet analysis of tide gauge at Charleston, New Zealand, 2680 km**  
 355 **away from the eruption site. The solid vertical white line marks the arrival time with travelling**  
 356 **velocity of 1000 m/s. The solid vertical red line marks the arrival of Lamb wave. The dashed**  
 357 **vertical white line marks lower limit of AGWs' velocity 200 m/s. The dashed vertical black line**  
 358 **marks the theoretical tsunami arrivals.**

359 An interesting phenomenon is that the tsunami component with 3–5 min period can still be observed in  
 360 a bay-shaped coastal area at Charleston in New Zealand (see the location in Figure 5) which is 2680 km  
 361 away from the eruption site and maintains a high energy level lasting up to 14 h (Figure 9b). The long-  
 362 traveling capability could be associated with the ~ 10000 m deep water depth of the Tonga Trench that  
 363 keeps the source signals from substantial attenuation. In deep open ocean, the wavelength of a tsunami  
 364 can reach two hundred kilometers, but the height of the tsunami may be only a few centimeters. Tsunami  
 365 waves in the deep ocean can travel thousands of kilometers at high speeds, meanwhile losing very little  
 366 energy in the process. The long oscillation can be attributed to the multiple reflections of the incoming  
 367 waves trapped in the shallow-water bay at Charleston.

368 Generally, devastating tsunamis with long-distance travelling capability are mostly generated by  
 369 megathrust earthquakes (Titov et al., 2005). Caldera collapses or submarine landslides with limited scale  
 370 normally only generate local tsunamis, e.g., the 1998 PNG (Papua New Guinea) tsunami event (Kawata

371 et al., 1999) and the 1930 Cabo Girão tsunami event (Ramalho et al., 2015). Therefore, it's exceptional  
372 that the tsunami component from scale-limited failure could travel at-least 2680 km away from the  
373 eruption site. It demonstrates that tsunamis from small-scale tsunamigenic source have the capability to  
374 travel long distance and cause long oscillation at favored condition, e.g., deep trench, ocean ridge and  
375 bay-shaped coasts.

#### 376 **4.2 The Possible Mechanisms of Long Tsunami Oscillation**

377 An important tsunami behavior of the 2022 HTHH tsunami is the long-lasting oscillation ~ 3 days in the  
378 Pacific Ocean (Figure 10a), which is comparable to that of the 2011 Tohoku tsunami, ~4 days  
379 (Heidarzadeh and Satake, 2013). We demonstrate the duration time of the tsunami oscillation through  
380 ARMS (Averaged-Root-Mean-Square) approach that is a measure of absolute average tsunami amplitude  
381 in a time period. The long-lasting tsunami energy can be observed at many regions, such as the coasts of  
382 New Zealand, Japan, Aleutian, Chile, Hawaii, and west coasts of America. Several mechanisms could  
383 account for the long-lasting tsunami, including (1) Lamb waves circling the Earth multiple times  
384 (Amores et al., 2022; Matoza et al., 2022), (2) resonance effect between ocean waves and atmospheric  
385 waves (Kubota et al., 2022), and (3) bathymetric effect. We discuss the contribution of each mechanism  
386 in the following section.

387 To investigate the contribution of Lamb wave to the long-lasting tsunami, we compare the air pressure  
388 disturbances recorded by selected barometers together with the tsunami waveforms of nearby tide gauges  
389 (Figure 10b). While the barometers present discernible wave pulses at each Lamb wave's arrival, only  
390 the first Lamb wave triggered clear tsunami signal and no detectable tsunami signatures correspond to  
391 the following passage, suggesting the Lamb waves do not directly contribute to the long oscillation.

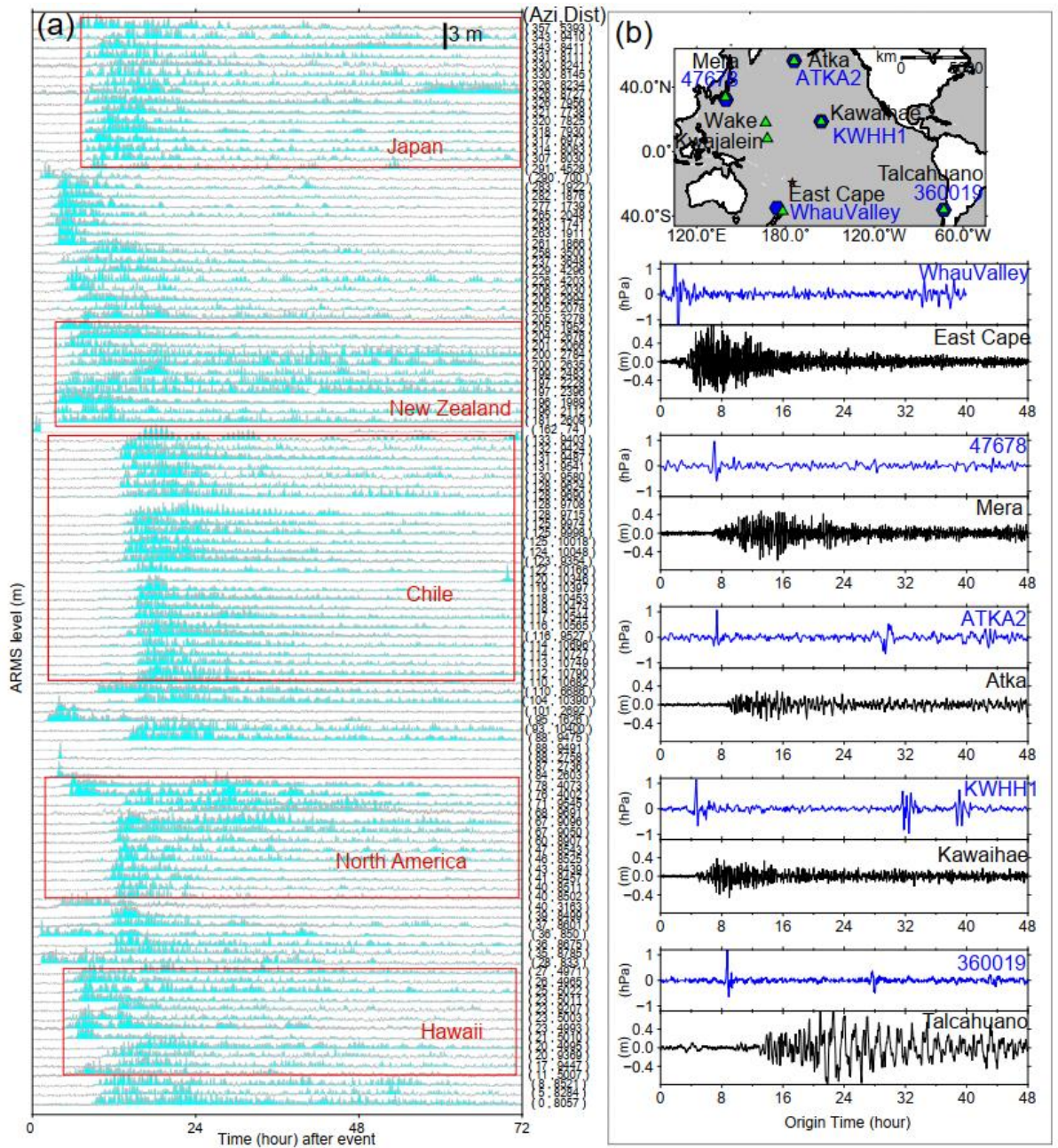
392 Theoretically, the resonance effects between ocean waves and atmospheric waves could contribute to the  
393 long oscillation on coastlines based on the following reasons. First, part of the atmospheric gravity waves  
394 propagated at velocities close to averaged velocities of conventional tsunami in the Pacific Ocean (198–  
395 221 m/s) which resulted in the resonance with ocean waves (Kubota et al., 2022). Second, when Lamb  
396 wave speed approaches the tsunami speed, Proudman resonance gradually increase tsunami heights,  
397 wherein Proudman resonance optimally maximizes tsunami heights when they match well. In deep  
398 oceanic trenches, such as Mariana and Tonga-Kermadec trench (10000–11000 m), tsunami velocities  
399 range between ~314–330m/s which are comparable with those of the observed Lamb waves 315–340

400 m/s. Therefore, the resonance effect could be a possible source of increased wave energy, especially in  
401 the deep trenches (Lynett et al., 2022; Tanioka et al., 2022).

402 To examine the role of local bathymetry in the long-lasting tsunami, we choose a well-studied and well-  
403 recorded event: the 2011 Mw 9.0 Tohoku tsunami as a reference event and compare the tsunami records  
404 of these two events at the same coastal stations. Although the two tsunami events were generated by  
405 completely different mechanisms, i.e., large-scale seafloor deformation for the Mw 9.0 megathrust  
406 earthquake (Mori et al., 2011) and fast-moving atmospheric waves for the Mw 5.8 volcanic eruption  
407 (Matoza et al., 2022), they both produced widespread transoceanic tsunamis which were well recorded  
408 in the Pacific DART buoys and tide gauges. In the near-field, the 2011 Tohoku earthquake produced  
409 runup up to 40 m at Miyako in the Iwate Prefecture, ~70 km from the source (Mori et al., 2011), while  
410 the 2022 HTHH tsunami produced only ~13 m runup in the near field from eyewitness accounts in  
411 Kanokupolu, 60 km from the volcano (Lynett et al., 2022). However, in the far-field (>1000 km), we  
412 observe comparable tsunami wave heights in certain coastal regions. Based on the tsunami records at 21  
413 tide gauges surrounding the Pacific Ocean, Heidarzadeh & Satake (2013) calculated the average value  
414 of the maximum tsunami heights (trough-to-crest) of the 2011 Tohoku tsunami is 1.6 m with the largest  
415 height of 3.9 m at the Coquimbo Bay in Chile (Heidarzadeh and Satake, 2013). Coincidentally, the statistics  
416 of 116 tide gauges in this study also suggest the average tsunami heights of the 2022 HTHH tsunami is  
417 around the same order, ~1.2 m, among which, the largest height is 3.6 m at Chañaral Bay in Chile.  
418 Interestingly, in the coastal region of South America, the locations of the largest tsunami heights of both  
419 events are adjacent (Figure 4a), i.e., Coquimbo (the 2011 Tohoku) and Chañaral (The 2022 HTHH).

420 To further compare the far-field hydrodynamic processes between these two events quantitatively, we  
421 conduct wavelet analysis for four representative tide gauges distributed across the Pacific Ocean, i.e.  
422 coastal gauges at East Cape in New Zealand, Kwajalein Island, Wake Island, and Talcahuaho in Chile  
423 (see their locations in Figures 10b). The temporal changes of tsunami energy of both events can be seen  
424 in Figure 11. At each tide gauge, the tsunami energy of the 2011 HTHH (Figure 11a) and the 2022 Tohoku  
425 tsunamis (Figure 11b) for the first few hours after the arrivals is nonuniform with different significant  
426 peaks distributed within a wide period band of ~3–100 min. Then, the following long-lasting energy of  
427 the both at each station presents similar pattern and is concentrated at identical and fairly narrower period  
428 channel, i.e., ~20–30 min at East Cape in New Zealand, ~40–60 min at Kwajalein Island, ~10 min at

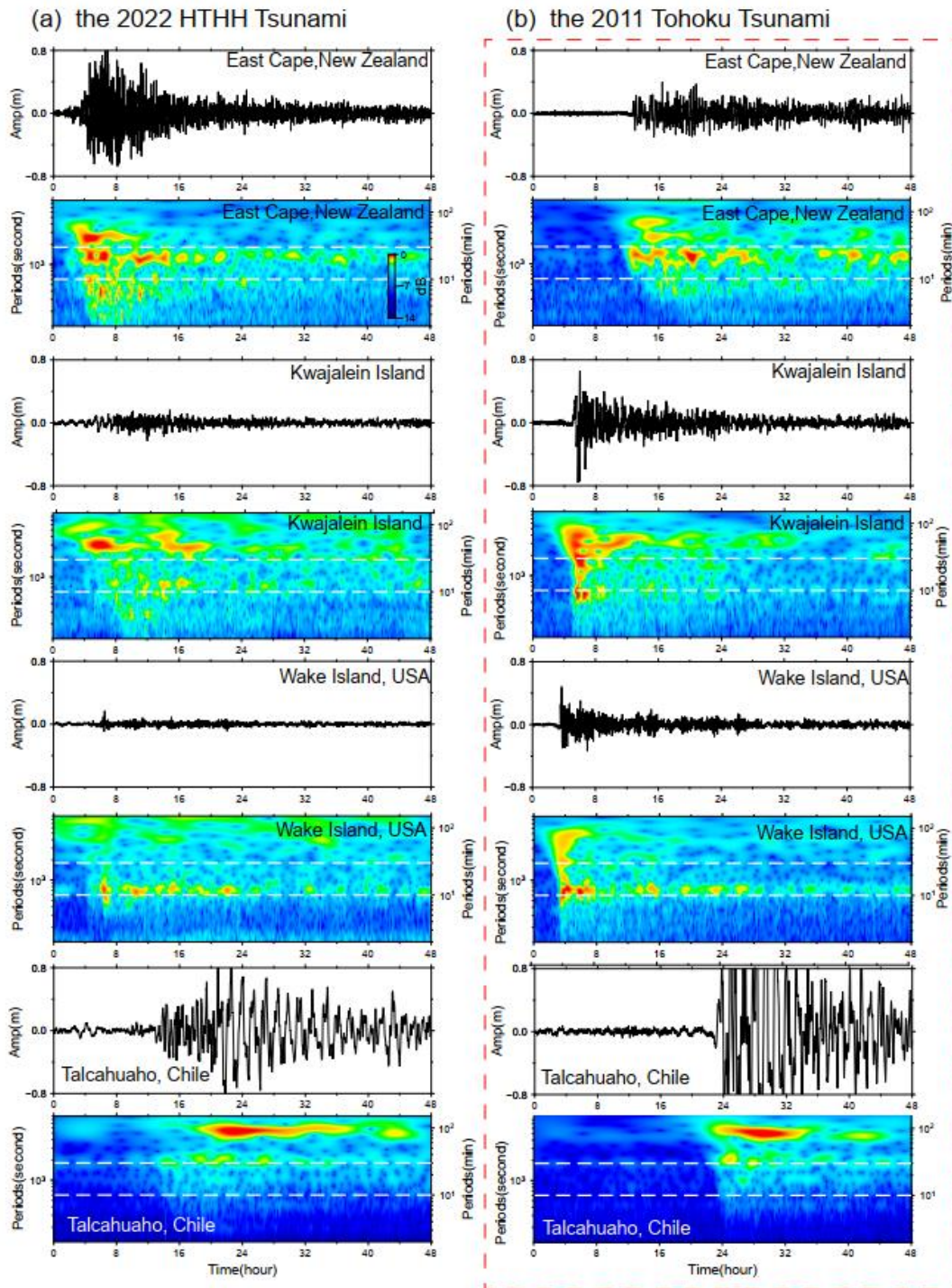
429 Wake Island, and ~100 min at Talcahuaho in Chile, which reflects the local bathymetric effects of natural  
430 permanent oscillations (Hu et al., 2022; Satake et al., 2020). Specifically, many bathymetric effects can  
431 contribute to the long-lasting tsunami, such as multiple reflections across the basins, or the continental  
432 shelves, and the excited tsunami resonance in bays/harbors with variable shapes and sizes (Aranguiz et  
433 al., 2019; Satake et al., 2020). For example, tide gauges around New Zealand are primarily distributed in  
434 harbors/ports with major natural oscillation modes of ~20–30 min (De Lange and Healy, 1986; Lynett et  
435 al., 2022). The first oscillation mode of central Chile is centered around ~100 min (Aranguiz et al., 2019).  
436 Consequently, Figure 11 illustrates that the long-lasting tsunami energy of the two events is respectively  
437 distributed in 20–30 min period at East Cape in New Zealand and in ~100 min period at Talcahuaho in  
438 central Chile. The coupling of bathymetric oscillation mode with tsunami containing similar-period wave  
439 results in the excitement of tsunami resonance, which amplifies tsunami waves and prolongs the tsunami  
440 oscillation at the two stations (Heidarzadeh et al., 2019, 2021; Hu et al., 2022; Wang et al., 2022).  
441 Simply put, we do not have clear evidence that atmospheric acoustic-gravity waves from the 2022 HTHH  
442 eruption directly contribute to the long-lasting tsunami, but the resonance effect associated with ocean  
443 waves could a possible source of increased wave energy and amplification. However, the similarity of  
444 far-field hydrodynamic behaviors between the 2022 HTHH volcanic tsunami and the 2011 Tohoku  
445 seismogenic tsunami well demonstrates the both went through similar hydrodynamic processes after their  
446 arrivals. The consistency favors that the long-lasting tsunami of 2022 HTHH tsunami event can very  
447 likely be attributed by the interplays between local bathymetry and conventional tsunami left after each  
448 passage of atmospheric waves, which can well explain why the two completely distinct tsunami events  
449 possess a comparable duration time.



450

451 **Figure 10. Tsunami duration. (a) Tsunami durations at Pacific 116 tide gauges through ARMS level**  
 452 **approach. (b) the location of barographs (blue curves) and nearby tide gauges (green curves), as**  
 453 **well as their waveforms.**

454



455  
 456 **Figure 11. Wavelet analysis of tsunami waveforms recorded by 4 tide gauges during (a) the 2022**  
 457 **HTHH tsunami event, and (b) the 2011 Tohoku tsunami event. Horizontal white dashed lines**  
 458 **respectively mark reference periods of 10 min and 30 min.**

459 **4.3 Challenges for Tsunami Warning**

460 The generation mechanisms and hydrodynamic characteristics of the 2022 HTHH volcanic tsunami are  
 461 more complicated than pure seismogenic tsunami, which challenge the traditional tsunami warning

462 approach.

463 The first challenge is posed by the tsunami components with propagating velocities faster than the  
464 conventional tsunami. The Tonga volcanic tsunami event provides an excellent example which highlights  
465 that the tsunamigenic mechanisms are not limited to tectonic activities related with the sudden seafloor  
466 displacements, but also include a variety of atmospheric waves with distinct propagation velocities. The  
467 tsunami components in 2022 HTHH event generated by the air-sea coupling possess a wide range of  
468 velocities from 1000 m/s to 200 m/s. The Lamb waves recorded in both the 2022 HTHH event and the  
469 1833 Krakatoa volcanic event traveled along the Earth's surface globally for several times (Carvajal et  
470 al., 2022). The tsunami waves produced by Lamb waves, the wave components associated with resonance  
471 of the air-sea coupling and their superimposition increase the difficulty of tsunami warning.

472 Another critical challenge is associated with the interplays between tsunami waves and local bathymetry.  
473 The tsunami waves left by each passage of the atmospheric waves can interact with local bathymetry at  
474 coastlines, such as continental shelves with different slopes, and harbor/bay with different shapes and  
475 sizes. The interaction can intensify the tsunami impact and excite a variety of natural oscillation periods.  
476 The 2022 HTHH tsunami with an extremely wide period range of ~2–100 min have a great potential to  
477 couple with the excited natural oscillations and form extensive tsunami resonance phenomena. The  
478 resonance effects result in long-lasting oscillation and delayed tsunami wave peaks. The uncertain  
479 arrivals of the maximum tsunami waves pose an extra challenge to tsunami warning.

## 4805. **Conclusion**

481 In the study, we explore the tsunamigenic mechanisms and the hydrodynamic characteristics of the 2022  
482 HTHH volcanic tsunami event. Through extensive analysis of waveforms recorded by the DART buoys,  
483 tide gauges and barometers in the Pacific Ocean, we reach the main findings as follows:

484 (1) We identify four distinct tsunami wave components based on their distinct propagation velocities or  
485 period bands (~80–100 min, 10–30 min, 30–40 min, and 3–5 min). The generation mechanisms of these  
486 tsunami components range from air-sea coupling to seafloor crustal deformation during the volcanic  
487 eruption.

488 (2) The first-arriving tsunami component with 80–100 min period was most likely from shock wave  
489 spreading at a velocity of ~1000 m/s in the vicinity of the eruption. This tsunami component was not

490 clearly identified by currently available publication and it's not easy to be visually observed through time  
491 series of the waveforms. The physical mechanism is yet to be understood. The second tsunami component  
492 with 30–40 min period was from Lamb waves, and was the most discussed tsunami source of this event  
493 so far. A thorough analysis of DART measurements indicates that the Lamb waves traveled at the speed  
494 of ~340 m/s in the vicinity of the eruption and decreased to ~315 m/s when traveling away due to cooling  
495 of the air temperature. The third tsunami component was from some atmospheric gravity wave modes  
496 with propagation velocity faster than 200 m/s but slower than Lamb waves. The last tsunami component  
497 with the shortest periods 3-5 min was probably produced by partial caldera collapse with estimated  
498 dimension of ~0.8–1.8 km.

499 (3) Although the resonance effect with the atmospheric acoustic-gravity waves theoretically could be a  
500 source of increased wave energy, its direct contribution to the long-lasting oscillation is not demonstrated  
501 yet. However, the comparison of hydrodynamical characteristics between the 2022 HTHH tsunami event  
502 and the 2011 Tohoku tsunami event well demonstrated that the interactions between the ocean waves left  
503 by atmospheric waves and local bathymetry contribute to the long-lasting Pacific oscillation of the 2022  
504 tsunami event.

505 (4) The extraordinary features of this rare volcanic tsunami event challenge the current tsunami warning  
506 system which is mainly designed for seismogenic tsunamis. It is necessary to improve the awareness of  
507 people at risks about the potential tsunami hazards associated with volcanic eruptions. New approaches  
508 are expected to be developed for tsunami hazard assessments with these unusual sources: various  
509 atmospheric waves radiated by volcanic eruptions besides those traditionally recognized, e.g.  
510 earthquakes, landslides, caldera collapses and pyroclastic flows etc.

## 511 **Acknowledgment**

512 This work was supported by National Natural Science Foundation (No 41976197, No 12002099),  
513 Innovation Group Project of Southern Marine Science and Engineering Guangdong Laboratory (Zhuhai)  
514 (No. 311021002), Key Research and Development Program of Hainan Province (No. ZDYF2020209),  
515 Southern Marine Science and Engineering Guangdong Laboratory (Zhuhai) (SML2021SP305) and  
516 Fundamental Research Funds for the Central Universities, Sun Yat-sen University (2021qntd23).

517 The JAGURS tsunami simulation code is employed for tsunami modelling (Baba et al., 2015;



518 <https://zenodo.org/record/6118212#.Yk98qdtBxPY>). Bathymetry data are obtained from GEBCO at  
519 <http://www.gebco.net>. The sea level records in deep ocean are available from the Deep Ocean Assessment  
520 and Reporting of Tsunamis (DART) buoy network in the Pacific (<https://nctr.pmel.noaa.gov/Dart/>), and  
521 GeoNet New Zealand DART network (<https://tilde.geonet.org.nz>). The sea level records of tide gauges  
522 are downloaded from UNESCO/ IOC (<http://www.ioc-sealevelmonitoring.org/>). Barometer data are  
523 provided by the following providers: Direccio'n Meteorolo'gica de Chile  
524 (<https://climatologia.meteochile.gob.cl>), NOAA National Weather Service  
525 (<https://www.weather.gov/ilm/observations>), Japan Meteorological Agency (<https://www.jma.go.jp>),  
526 The UK Met Office Weather Observation (<https://www.metoffice.gov.uk/observations>), and Fiji  
527 Meteorological Service (<https://www.met.gov.fj>).

## 528 **Reference**

- 529 Adam, D.: Tonga volcano created puzzling atmospheric ripples, *Nature*,  
530 <https://doi.org/10.1038/d41586-022-00127-1>, 2022.
- 531 Amores, A., Monserrat, S., Marcos, M., Argüeso, D., Villalonga, J., Jordà, G., and Gomis, D.:  
532 Numerical simulation of atmospheric Lamb waves generated by the 2022 Hunga-Tonga volcanic  
533 eruption, *Geophys. Res. Lett.*, 49, e2022GL098240, <https://doi.org/10.1029/2022GL098240>, 2022.
- 534 Aranguiz, R., Catalán, P. A., Cecioni, C., Bellotti, G., Henriquez, P., and González, J.: Tsunami  
535 Resonance and Spatial Pattern of Natural Oscillation Modes With Multiple Resonators, *J. Geophys.*  
536 *Res. Ocean.*, 124, 7797–7816, <https://doi.org/10.1029/2019JC015206>, 2019.
- 537 Baba, T., Takahashi, N., Kaneda, Y., Ando, K., Matsuoka, D., and Kato, T.: Parallel Implementation of  
538 Dispersive Tsunami Wave Modeling with a Nesting Algorithm for the 2011 Tohoku Tsunami, *Pure*  
539 *Appl. Geophys.*, 172, 3455–3472, <https://doi.org/10.1007/s00024-015-1049-2>, 2015.
- 540 Bevis, M., Taylor, F. W., Schutz, B. E., Recy, J., Isacks, B. L., Helu, S., Singh, R., Kendrick, E.,  
541 Stowell, J., Taylor, B., and Calmantli, S.: Geodetic observations of very rapid convergence and back-  
542 arc extension at the tonga arc, *Nature*, 374, 249–251, <https://doi.org/10.1038/374249a0>, 1995.
- 543 Billen, M. I., Gurnis, M., and Simons, M.: Multiscale dynamics of the Tonga–Kermadec subduction  
544 zone, *Geophys. J. Int.*, 153, 359–388, <https://doi.org/10.1046/j.1365-246X.2003.01915.x>, 2003, 2003.
- 545 Carvajal, M., Sepúlveda, I., Gubler, A., and Garreaud, R.: Worldwide Signature of the 2022 Tonga

546 Volcanic Tsunami, *Geophys. Res. Lett.*, 49, e2022GL098153, <https://doi.org/10.1029/2022GL098153>,  
547 2022.

548 Duncombe, J.: The Surprising Reach of Tonga’s Giant Atmospheric Waves.pdf, *Eos (Washington*  
549 *DC)*, 103, <https://doi.org/10.1029/2022EO220050>, 2022.

550 E. E. Gossard and W. H. Hooke: *Waves in the Atmosphere: Atmospheric Infrasound and Gravity*  
551 *Waves—Their Generation and Propagation*, Elsevier, 1975.

552 Edmonds, M.: Hunga-Tonga-Hunga-Ha’apai in the south Pacific erupts violently, *Temblor*,  
553 <https://doi.org/10.32858/temblor.231>, 2022.

554 Garvin, J. B., Slayback, D. A., Ferrini, V., Frawley, J., Giguere, C., Asrar, G. R., and Andersen, K.:  
555 Monitoring and Modeling the Rapid Evolution of Earth’s Newest Volcanic Island: Hunga Tonga  
556 Hunga Ha’apai (Tonga) Using High Spatial Resolution Satellite Observations, *Geophys. Res. Lett.*, 45,  
557 3445–3452, <https://doi.org/10.1002/2017GL076621>, 2018.

558 Gossard, E. E. and Hooke, W. H.: *Waves in the Atmosphere*, Amsterdam: Elsevier, 1975.

559 Heidarzadeh, M. and Satake, K.: Waveform and Spectral Analyses of the 2011 Japan Tsunami Records  
560 on Tide Gauge and DART Stations Across the Pacific Ocean, *Pure Appl. Geophys.*, 170, 1275–1293,  
561 <https://doi.org/10.1007/s00024-012-0558-5>, 2013.

562 Heidarzadeh, M. and Satake, K.: Excitation of Basin-Wide Modes of the Pacific Ocean Following the  
563 March 2011 Tohoku Tsunami, *Pure Appl. Geophys.*, 171, 3405–3419, [https://doi.org/10.1007/s00024-](https://doi.org/10.1007/s00024-013-0731-5)  
564 [013-0731-5](https://doi.org/10.1007/s00024-013-0731-5), 2014.

565 Hu, G., Feng, W., Wang, Y., Li, L., He, X., Karakaş, Ç., and Tian, Y.: Source characteristics and  
566 exacerbated tsunami hazard of the 2020 Mw 6.9 Samos earthquake in eastern Aegean Sea, *J. Geophys.*  
567 *Res. Solid Earth*, 127, e2022JB023961, <https://doi.org/10.1029/2022JB023961>, 2022.

568 Kawata, Y., Benson, B. C., Borrero, J. C., Borrero, J. L., Davies, H. L., Lange, W. P. de, Imamura, F.,  
569 Letz, H., Nott, J., and Synolakis, C. E.: Tsunami in Papua New Guinea Was as Intense as First  
570 Thought, *Eos, Trans. Am. Geophys. Union*, 80, 9, <https://doi.org/10.1029/99EO00065>, 1999.

571 Kristeková, M., Kristek, J., Moczo, P., and Day, S. M.: Misfit Criteria for Quantitative Comparison of  
572 Seismograms, *Bull. Seismol. Soc. Am.*, 96, 1836–1850, <https://doi.org/10.1785/0120060012>, 2006.

573 Kubota, T., Saito, T., and Nishida, K.: Global fast-traveling tsunamis by atmospheric pressure waves  
574 on the 2022 Tonga eruption, *Science (80-. )*, <https://doi.org/10.1126/science.abo4364>, 2022.

575 Kulichkov, S. N., Chunchuzov, I. P., Popov, O. E., Gorchakov, G. I., Mishenin, A. A., Perepelkin, V.  
576 G., Bush, G. A., Skorokhod, A. I., Yu. A. Vinogradov, Semutnikova, E. G., Šepic, J., Medvedev, I. P.,  
577 Gushchin, R. A., Kopeikin, V. M., Belikov, I. B., Gubanova, D. P., and A. V. Karpov & A. V.  
578 Tikhonov: Acoustic-Gravity Lamb Waves from the Eruption of the Hunga-Tonga-Hunga-Hapai  
579 Volcano, Its Energy Release and Impact on Aerosol Concentrations and Tsunami, *Pure Appl.*  
580 *Geophys.*, <https://doi.org/10.1007/s00024-022-03046-4>, 2022.

581 De Lange, W. P. and Healy, T. R.: New Zealand tsunamis 1840–1982, *New Zeal. J. Geol. Geophys.*,  
582 29, 115–134, <https://doi.org/10.1080/00288306.1986.10427527>, 1986.

583 Lin, J., Rajesh, P. K., Lin, C. C. H., Chou, M., Liu, J.-Y., Yue, J., Hsiao, T.-Y., Tsai, H.-F., Chao, H.-  
584 M., and Kung, M.-M.: Rapid Conjugate Appearance of the Giant Ionospheric Lamb Wave Signatures  
585 in the Northern Hemisphere After Hunga- Tonga Volcano Eruptions, *Geophys. Res. Lett.*, 49,  
586 e2022GL098222, <https://doi.org/10.1029/2022GL098222>, 2022.

587 Liu, P. L.-F. and Higuera, P.: Water waves generated by moving atmospheric pressure : Theoretical  
588 analyses with applications to the 2022 Tonga event, *arXiv Prepr.*,  
589 <https://doi.org/10.48550/arXiv.2205.05856>, 2022.

590 Liu, X., Xu, J., Yue, J., and Kogure, M.: Strong Gravity Waves Associated With Tonga Volcano  
591 Eruption Revealed by SABER Observations, *Geophys. Res. Lett.*, 49, e2022GL098339,  
592 <https://doi.org/10.1029/2022GL098339>, 2022.

593 Lynett, P., McCann, M., Zhou, Z., Renteria, W., Borrero, J., Greer, D., Fa'anunu, 'Ofa, Bosserelle, C.,  
594 Jaffe, B., Selle, S. La, Ritchie, A., Snyder, A., Nasr, B., Bott, J., Graehl, N., Synolakis, C., Ebrahimi,  
595 B., and Cinar, E.: The Tsunamis Generated by the Hunga Tonga- Hunga Ha 'apai Volcano on January  
596 15 , 2022, *ResearchSquare*, <https://doi.org/10.21203/rs.3.rs-1377508/v1>, 2022.

597 Matoza, R. S., Matoza, R. S., Fee, D., Assink, J. D., Iezzi, A. M., Green, D. N., Kim, K., Lecocq, T.,  
598 Krishnamoorthy, S., Lalande, J., Nishida, K., and Gee, K. L.: Atmospheric waves and global  
599 seismoacoustic observations of the January 2022 Hunga eruption ,Tonga, *Science (80-. )*,  
600 <https://doi.org/10.1126/science.abo7063>, 2022.

601 Mori, N., Takahashi, T., Yasuda, T., and Yanagisawa, H.: Survey of 2011 Tohoku earthquake tsunami  
602 inundation and run-up, *Geophys. Res. Lett.*, 38, L00G14, <https://doi.org/10.1029/2011GL049210>,  
603 2011.

604 NASA: National Aeronautics and Space Administration, “Dramatic changes at Hunga Tonga-Hunga  
605 Ha’apai,” 2022.

606 Nomanbhoy, N. and Satake, K.: Generation mechanism of tsunamis from the 1883 Krakatau Eruption,  
607 *Geophys. Res. Lett.*, 22, 509–512, <https://doi.org/10.1029/94GL03219>, 1995.

608 Omira, R., Baptista, M. A., Quartau, R., Ramalho, R. S., Kim, J., Ramalho, I., and Rodrigues, A.: How  
609 hazardous are tsunamis triggered by small-scale mass-wasting events on volcanic islands ? New  
610 insights from Madeira–NE Atlantic, *Earth Planet. Sci. Lett.*, 578, 117333,  
611 <https://doi.org/10.1016/j.epsl.2021.117333>, 2022.

612 Otsuka, S.: Visualizing Lamb Waves From a Volcanic Eruption Using Meteorological Satellite  
613 Himawari-8, *Geophys. Res. Lett.*, 49, e2022GL098324, <https://doi.org/10.1029/2022GL098324>, 2022.

614 Pelinovsky, E., Choi, B. H., Stromkov, A., Didenkulova, I., and Kim, H.: Analysis of Tide-Gauge  
615 Records of the 1883 Krakatau Tsunami. In: Satake, K. (eds) *Tsunamis*, *Adv. Nat. Technol. Hazards*  
616 *Res.*, 23, Springer, Dordrech, [https://doi.org/10.1007/1-4020-3331-1\\_4](https://doi.org/10.1007/1-4020-3331-1_4), 2005.

617 Plank, S., Marchese, F., Genzano, N., Nolde, M., and Martinis, S.: The short life of the volcanic island  
618 New Late’iki (Tonga) analyzed by multi-sensor remote sensing data, *Sci. Rep.*, 10, 22293,  
619 <https://doi.org/10.1038/s41598-020-79261-7>, 2020.

620 Rabinovich, A. B.: Spectral analysis of tsunami waves: Separation of source and topography effects, *J.*  
621 *Geophys. Res. Ocean.*, 102, 12663–12676, <https://doi.org/10.1029/97JC00479>, 1997.

622 Rabinovich, A. B.: Seiches and harbor oscillations. in: *Handbook of coastal and ocean engineering*, pp,  
623 193–236, 2009.

624 Rabinovich, A. B., Thomson, Æ. R. E., and Stephenson, F. E.: The Sumatra tsunami of 26 December  
625 2004 as observed in the North Pacific and North Atlantic oceans, *Surv. Geophys.*, 27, 647–677,  
626 <https://doi.org/10.1007/s10712-006-9000-9>, 2006.

627 Rabinovich, A. B., Titov, V. V., Moore, C. W., and Eble, M. C.: The 2004 Sumatra Tsunami in the  
628 Southeastern Pacific Ocean: New Global Insight From Observations and Modeling, *J. Geophys. Res.*  
629 *Ocean.*, 122, 7992–8019, <https://doi.org/https://doi.org/10.1002/2017JC013078>, 2017.

630 Ramalho, R. S., Winckler, G., Madeira, J., Helffrich, G. R., Hipólito, A., Quartau, R., Adena, K., and  
631 Schaefer, J. M.: Hazard potential of volcanic flank collapses raised by new megatsunami evidence, *Sci.*  
632 *Adv.*, 1, e1500456, <https://doi.org/10.1126/sciadv.1500456>, 2015.

633 Ramírez-Herrera, M. T., Coca, O., and Vargas-Espinosa, V.: Tsunami Effects on the Coast of Mexico  
634 by the Hunga Tonga-Hunga Ha'apai Volcano, *Pure Appl. Geophys.*, [https://doi.org/10.1007/s00024-](https://doi.org/10.1007/s00024-022-03017-9)  
635 [022-03017-9](https://doi.org/10.1007/s00024-022-03017-9), 2022.

636 Satake, K.: Earthquakes: Double trouble at Tonga, *Nature*, 466, 931–932,  
637 <https://doi.org/10.1038/466931a>, 2010.

638 Satake, K., Heidarzadeh, M., Quiroz, M., and Cienfuegos, R.: History and features of trans-oceanic  
639 tsunamis and implications for paleo-tsunami studies, *Earth-Science Rev.*, 202, 103112,  
640 <https://doi.org/10.1016/j.earscirev.2020.103112>, 2020.

641 Self, S. and Rampino, M. R.: K-1981Self\_Nature\_The 1883 eruption of Krakatau, *Nature*, 294, 699–  
642 704, <https://doi.org/10.1038/294699a0>, 1981.

643 Stern, S., Cronin, S., Ribo, M., Barker, S., Brenna, M., Smith, I. E. M., Ford, M., Kula, T., and  
644 Vaiomounga, R.: Post-2015 caldera morphology of the Hunga Tonga-Hunga Ha 'apai caldera ,  
645 Tonga , through drone photogrammetry and summit area bathymetry, *EGU Gen. Assem.* 2022,  
646 <https://doi.org/10.5194/egusphere-egu22-13586>, 2022.

647 Tanioka, Y., Yamanaka, Y., and Nakagaki, T.: Characteristics of the deep sea tsunami excited offshore  
648 Japan due to the air wave from the 2022 Tonga eruption, *Earth, Planets Sp.*, 74, 61,  
649 <https://doi.org/10.1186/s40623-022-01614-5>, 2022.

650 Themens, D. R., Watson, C., Žagar, N., Vasylykevych, S., Elvidge, S., McCaffrey, A., Prikryl, P., Reid,  
651 B., Wood, A., and Jayachandran, P. T.: Global Propagation of Ionospheric Disturbances Associated  
652 With the 2022 Tonga Volcanic Eruption, *Geophys. Res. Lett.*, 49, e2022GL098158,  
653 <https://doi.org/10.1029/2022GL098158>, 2022.

654 Titov, V., Rabinovich, A. B., Mofjeld, H. O., Thomson, R. E., and Gonza, F. I.: The Global Reach of  
655 the 26 December 2004 Sumatra Tsunami, *Science (80-. )*, 309, 2045–2049,  
656 <https://doi.org/10.1126/science.1114576>, 2005.

657 USGS: M 5.8 Volcanic Eruption - 68 km NNW of Nuku'alofa, Tonga, *U.S. Geol. Surv.*, 2022.

658 Wang, Y., Heidarzadeh, M., Satake, K., Mulia, I. E., and Yamada, M.: A Tsunami Warning System  
659 Based on Offshore Bottom Pressure Gauges and Data Assimilation for Crete Island in the Eastern  
660 Mediterranean Basin, *J. Geophys. Res. Solid Earth*, 125, e2020JB020293,  
661 <https://doi.org/10.1029/2020JB020293>, 2020.

662 Wang, Y., Zamora, N., Quiroz, M., Satake, K., and Cienfuegos, R.: Tsunami Resonance  
663 Characterization in Japan Due to Trans-Pacific Sources: Response on the Bay and Continental Shelf, *J.*  
664 *Geophys. Res. Ocean.*, 126, 1–16, <https://doi.org/10.1029/2020JC017037>, 2021.

665 Wang, Y., Heidarzadeh, M., Satake, K., and Hu, G.: Characteristics of two tsunamis generated by  
666 successive Mw 7.4 and Mw 8.1 earthquakes in Kermadec Islands on March 4,2021, *Nat. Hazards Earth*  
667 *Syst. Sci.*, 22, 1–10, <https://doi.org/10.5194/nhess-2021-369>, 2022.

668 Yuen, D. A., Scruggs, M. A., Spera, F. J., Yingcai Zheng, Hao Hu, McNutt, S. R., Glenn Thompson,  
669 Mandli, K., Keller, B. R., Wei, S. S., Peng, Z., Zhou, Z., Mulargia, F., and Tanioka1, Y.: Under the  
670 Surface: Pressure-Induced Planetary-Scale Waves, Volcanic Lightning, and Gaseous Clouds Caused by  
671 the Submarine Eruption of Hunga Tonga-Hunga Ha’apai Volcano Provide an Excellent Research  
672 Opportunity, *Earthq. Res. Adv.*, <https://doi.org/10.1016/j.eqrea.2022.100134>, 2022.

673 Zhang, S., Vierinen, J., Aa, E., Goncharenko, L. P., Erickson, P. J., Rideout, W., Coster, A. J., and  
674 Spicher, A.: 2022 Tonga Volcanic Eruption Induced Global Propagation of Ionospheric Disturbances  
675 via Lamb Waves, *Front. Astron. Sp. Sci.*, 9, 1–10, <https://doi.org/10.3389/fspas.2022.871275>, 2022.

676